UC Berkeley
UC Berkeley Previously Published Works

Title
Embedded boundary methods for modeling 3D finite-difference Laplace-Fourier domain acoustic-wave equation with free-surface topography

Permalink
https://escholarship.org/uc/item/97t995qq

Journal
Geophysics, 83(5)

ISSN
0016-8033

Authors
AlSalem, Hussain
Petrov, Petr
Newman, Gregory
et al.

Publication Date
2018-09-01

DOI
10.1190/geo2017-0828.1

Peer reviewed

Embedded boundary methods for modeling 3D finite-difference Laplace-Fourier domain acoustic-wave equation with free-surface topography

Hussain AlSalem[1], Petr Petrov[2], Gregory Newman[2] and James Rector[1]

[1]University of California-Berkeley, Department of Civil and Environmental Engineering, 2594 Hearst Ave, Berkeley, California 94709, USA. E-mail: hjirms@gmail.com; jwrector@lbl.gov.

[2]Lawrence Berkeley National Laboratory, 67 Centennial Dr, Berkeley, California 94705, USA. E-mail: pvpetrov@lbl.gov; ganewman@lbl.gov.

Abstract

We have developed embedded boundary methods to handle arbitrarily shaped topography to accurately simulate acoustic seismic wave propagation in the Laplace-Fourier domain. The purpose is to use this method to enhance accurate wave simulation near the surface. Unlike most existing methods such as the ones using curvilinear grids to fit irregular surface topography, we use a regular Cartesian grid system without suffering from the staircasing error that occurs in conventional implementations. In this improved embedded-boundary method, we use the method of images, by imposing ghost nodes above the surface and approximating their acoustic pressures using linear extrapolation, quadratic interpolation, or cubic interpolation, to account for an arbitrarily curved surface. Implementing this method instead of using curvilinear grids near the boundaries greatly reduces the complexity of preprocessing procedures and the computational cost. Furthermore, using numerical examples, we found the accuracy gain and performance of our embedded-boundary methods in comparison with conventional finite-difference implementation of the problem.

Keywords: acoustic, 3D, finite difference, frequency domain, modeling

Introduction

In acoustic seismic modeling, the objective is to describe the propagation of waves through the earth. Here, we consider wave propagation that is solved in the Laplace-Fourier domain. We start by discretizing the 3D wave equation on a Cartesian grid $x_{i,j,k}=(ih,jh,kh)$ in space, where $h>0$ is the grid size. We let the Laplace frequency be complex valued $s=\sigma+i\omega$ consisting of a Laplace damping factor σ and the angular frequency ω. The solution to the forward problem is gained by using a single frequency for a 3D acoustic-wave simulation (Hustedt et al., 2004). It is reduced from the 3D elastic wavefield simulator developed by Petrov and Newman (2012).

Special attention to the numerical treatment of the free-surface boundary for topography is deserved because it does not follow naturally from a Cartesian grid. For acoustic forward modeling, second-order finite-difference methods do not implicitly satisfy the free-surface condition as is the case with finite-

element methods. Accurately implementing the free-surface condition on an irregular interface is difficult due to the nonlocal nature of the finite-difference schemes. This implies that acoustic velocities above the free surface are required to compute the pressure at or immediately below the surface (Fichtner, 2011).

A straightforward approach for the implementation of the free surface is to set the acoustic parameters at and above the free surface to zero. The method is commonly referred to as vacuum formulation or the staircase method. The free-surface boundary condition is thus not treated explicitly; instead, it is assumed to be implicitly fulfilled. Staircase-method applications can be found in Zahradník and Urban (1984), Zahradník et al. (1993), and Ohminato and Chouet (1997). The method is attractive because of its trivial implementation and the possibility to model topography. Bohlen and Saenger (2006) conclude that to model topography with a staircase method, more than 60 grid points per minimum wavelength are required in a second-order scheme to obtain acceptable results.

Another solution is the curvilinear method that transforms the velocity-pressure formulation system of equations from a curved to a rectangular grid (Tessmer et al., 1992; Tessmer and Kosloff, 1994; Hestholm, 1999; Hestholm and Ruud, 2000). At the free surface, the pressure and velocities are transformed into local systems in which the vertical coordinate axis is parallel to the normal of the local surface element. The free-surface conditions are then implemented by a "characteristic" treatment of the velocity and pressure components, before they are rotated back to the original system. More recent studies applied the embedded-boundary condition for a 2D finite-difference solution of the wave equation with success (Kreiss and Petersson, 2006; Li et al., 2010). The studies applied the embedded-boundary method to 2D frequency- and time-domain modeling problems. They investigate quadratic interpolation when computing the pressure above the free surface.

This paper describes an embedded-boundary method for the 3D acoustic-wave equation with an irregular free-surface boundary on a Cartesian grid. By computing the pressure on either side of the interface, we can satisfy a zero acoustic pressure at the free surface, yielding superior results compared with conventional implementations that model topography as a staircase approximation.

ACOUSTIC-WAVE EQUATION FORWARD MODELING IN LAPLACE-FOURIER DOMAIN

requency-domain modeling of wave propagation inside the earth has been studied extensively (see Lysmer and Drake, 1972; Marfurt, 1984; Zahradník and Urban, 1984; Pratt and Worthington, 1990; Jo et al., 1996; Štekl and Pratt, 1998; Hustedt et al., 2004; Operto et al., 2007). Most of the methods that have been developed for wave modeling in the frequency domain are based on solving the acoustic-wave equation by the finite-difference method:

On a uniform grid, the finite-difference methods provide an excellent compromise between accuracy and computational efficiency.

We consider the first-order hyperbolic system in a velocity-pressure formulation in the Laplace-Fourier domain, which can be derived from Petrov and Newman (2012). Let the 3D isotropic acoustic medium with density ρ and incompressibility κ occupy region Ω. The equations of motion inside Ω are given by

$$s\rho v_x = \partial_x P,$$
$$s\rho v_y = \partial_y P,$$
$$s\rho v_z = \partial_z P,$$
$$sP = \kappa[\partial_x v_x + \partial_y v_y + \partial_z v_z] + sm,$$

(1)

where s is the complex number given by σ+iω, σ is the Laplace damping factor, ω is the angular frequency, and $i=\sqrt{-1}$. The velocities v_x, v_y, and v_z are the velocity wavefield components; P is the acoustic pressure; m is the seismic moment density tensor; and the symbols ∂_x, ∂_y, and ∂_z denote the partial differential operators $\partial/\partial x$, $\partial/\partial y$, and $\partial/\partial z$, respectively. The Laplace-Fourier equations of motion (equation 1) are obtained by transforming the time-domain system of equations (Virieux, 1986) using the following Laplace-Fourier transform:

$$g(s) = \int_0^\infty g(t)e^{-st}dt,$$

(2)

where g(t) includes the functions vx(t), vy(t), vz(t), and P(t).

For the numerical solution of equation 1, we used second- and fourth-order finite-difference schemes with 7 and 13 point stencils, respectively (Petrov and Newman, 2012). This system of equations must be augmented with boundary conditions. In the case of infinite media, the nonreflecting condition for wavefield components is applied at the boundaries of region Ω. We used the perfectly matched layer boundary conditions (Hastings et al., 1996; Kim and Pasciak, 2010). However, at a free-surface boundary, one needs to incorporate the following boundary:

$$P=0.$$

(3)

In simple topography settings, in which the free surface is a flat plane that coincides with the top plane of the finite-difference grid, this boundary condition may be realized without any staircasing error (Graves, 1996; Gottschammer and Olsen, 2001). However, when the free surface has a more complicated geometric structure, incorporating the free-surface boundary condition becomes more challenging because the finite-difference

stencil will cross over the free surface as illustrated in Figure 1. In this setting, some algorithms perform adaptation of the finite-difference grid to the free surface (Hestholm, 1999; Hestholm and Ruud, 2000; Zhang and Chen, 2006; Zhang et al., 2012) or to construct the values of the wavefield on the exterior nodes if one wishes to keep the grid intact (Kreiss and Petersson, 2006; Lombard et al., 2008; Li et al., 2010).
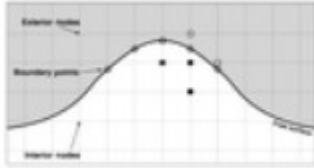

Figure 1. Smooth curved free surface on a uniform Cartesian grid for a second-order finite-difference stencil. The white squares denote the ghost nodes required by the stencil, the black squares denote the stencil interior grid nodes, and the circles denote the points on the free surface that are boundary points.

EMBEDDED BOUNDARY METHOD

e consider a case in which the free surface is immersed within a regular finite-difference grid and assume a homogeneous media around the boundary. The free surface can be defined by the equation

$$Zs=f(x,y). Zs=f(x,y). \tag{4}$$

We define grid nodes as interior nodes if they are inside the domain Ω and underneath the free surface, as shown in Figure 1. Nodes outside the domain of interest, i.e., above the free surface, are defined as exterior nodes, and points on the free-surface boundary are defined as boundary points. The ghost nodes are defined to be grid points outside the domain of interest but still being requested by stencils. For example, the second-order finite-difference scheme with seven stencil points requires only one layer of nodes above the surface (Figure 1).

With the above definitions, the problem of free-surface boundary treatment becomes the problem of updating the wavefield at the ghost nodes such that the wavefield at boundary points is forced to be zero according to the boundary condition in equation 3. Because we know the exact values of the pressure at the boundary, the boundary condition may be realized as extrapolation or interpolation of the wavefield from the interior nodes to the ghost nodes via the boundary points. This method is called the embedded boundary method (Kreiss and Petersson, 2006; Lombard et al., 2008; Li et al., 2010).

The value of the pressure at the ghost nodes may be defined by the method of images (Griffiths, 2005; Jackson, 2007). For each ghost node Pg, we define a ghost mirror point Pg,m below the surface inside the medium, where

$$P_g = -P_{g,m}. \tag{5}$$

The position and value of the ghost mirror Pg,m is defined by the distance from the surface and the surface form. For planar or spherical boundaries, the method of images ensures the realization of an exact boundary condition (Morse and Feshbach, 1954). Thus, it is widely used for the free-surface boundary condition with a flat surface (Levander, 1988; Graves, 1996). For an arbitrary boundary, it becomes an approximation. However, when the distance between the ghost node and the boundary is essentially smaller than the wavelength and the radius of the curvature, the boundary may be considered as locally planar or spherical. Because realistic topography always has some curvature, we can assume the surface near each ghost node is part of some sphere. This assumption is more general than the planar form because it allows us to include the curvature in the definition of the position and value of the ghost mirror Pg,m. Furthermore, the spherical form goes to the planar form when the radius of the curvature goes to infinity. Nodes above the ghost nodes that are not required by stencils are set to zero.

Ghost mirrors location

To locate the position of the ghost mirror, we find the closest distance between each ghost node at (xg,yg,zg) and its interpolated surface f(x,y) (see Appendix A). By considering the normal vector from the surface and the vector between the closest point on the surface and ghost node, we get the following system of nonlinear equations:

$$\begin{cases} x - x_g + \partial_x f(x, y)[f(x, y) - z_g] = 0 \\ y - y_g + \partial_y f(x, y)[f(x, y) - z_g] = 0. \end{cases} \tag{6}$$

By solving the system for x and y using the steepest-descent method, we attain the location of the closest point at the surface relative to the ghost node (Rheinboldt, 1998). According to Figure 2, the normal is extended a distance ξR from the closest point at the boundary into the subsurface to locate ghost mirror Pg,m.
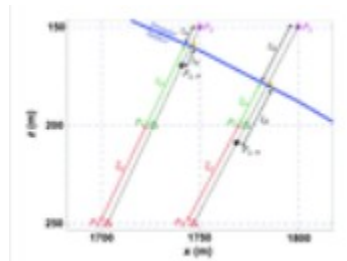

Figure 2. The 2D *y*-axis slice from the 3D second-order staggered grid. The blue line denotes the irregular surface, the black dashed line denotes the irregular surface normal at each ghost point, the magenta stars denote the ghost nodes, the orange squares denote the closest point in the surface that is normal to the ghost node, the black stars denote the ghost mirrors, the green and red triangles denote the known acoustic pressures, and ξRξR, ξDξD, and ξIξI are the relative distances. The nodes have 50 m grid spacing.

For a planar free surface, the distance ξ_R between P_g and the surface is equivalent to the distance $\xi'_{R'}$ between $P_{g,m}$ and the surface. However, if the surface is curved, the two distances (ξ_R and ξ'_R) are not equal (Figure 3). Our algorithm accounts for curvature of the surface and corrects the location of the ghost mirror $P_{g,m}$ by assuming the free surface is locally spherical. Because we know the approximated topography f, we can find the mean radius for the curvature using

$$R=-2\nabla\cdot\hat{n} =2\cdot(1+(\partial xf)2+(\partial yf)2)3/2(1+(\partial xf)2)\partial yyf-2\partial xf\partial yf\partial xyf+(1+(\partial yf)2)\partial xxf, \tag{7}$$

where $\hat{n}$ is the normal to the local surface f (Spivak, 1981). For the hill case in Figure 3a, the radius value is positive, whereas it is negative for the valley case in Figure 3b. The distance a between the curvature origin O and ghost node P_g can be found by

$$a = \begin{cases} R + \xi_R & \text{for } R > 0 \\ |R| - \xi_R & \text{for } R < 0 \end{cases}, \tag{8}$$

the distance ξ'_R between the ghost mirror $P_{g,m}$ and the surface is found using

$$\xi'_R = R\left(1 - \frac{|R|}{a}\right), \tag{9}$$

and the ghost node P_g is related to the ghost mirror $P_{g,m}$ by

$$(a|R|)P_{g,m}, \tag{10}$$

where R is the radius of the curvature. For planar and curved surfaces, the acoustic pressure value at the ghost mirror $P_{g,m}$ is necessary.
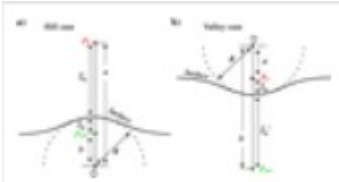

Figure 3. Method of images implementation. The red dot denotes the location of the ghost node, the green dot denotes the updated location of the ghost mirror due to the curved surface, RR denotes the radius of the curvature, $\xi_R\xi_R$ is the distance between the ghost node P_gP_g and the surface, $\xi'_R\xi_{R'}$ is the distance between the ghost mirror $P_{g,m}P_{g,m}$ and the surface, aa is the distance between the curvature origin OO and the ghost node P_gP_g, and bb is the distance between the curvature origin OO and the ghost mirror $P_{g,m}P_{g,m}$.

Second-order scheme implementation

To calculate the acoustic pressure at the ghost mirror points $P_{g,m}$, we consider interpolation and extrapolation methods. Thus, the acoustic pressure at the first layer PI and the acoustic pressure at the second layer PII below the surface are needed (see Figure 2). We know the acoustic pressure

at the surface to be zero, and the acoustic pressure at PI and PII can be approximated using bilinear interpolation. We either use linear extrapolation, quadratic interpolation, or a hybrid method to calculate acoustic pressures at ghost mirror points Pg,m and hence their corresponding ghost nodes Pg (see Figure 2).

Quadratic interpolation needs three points to determine the ghost mirror acoustic pressure Pg,m. Figure 4 shows that to approximate the acoustic pressure of ghost nodes Pg, we use Lagrange quadratic interpolation on values 0, PI, and PII at locations 0, ξD, and ξD+ξI (Li et al., 2010). To improve the accuracy of the quadratic interpolation, we use linear extrapolation.
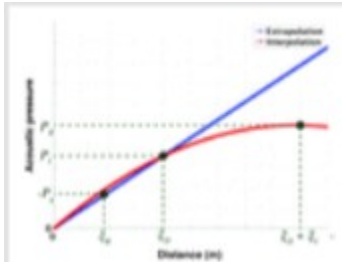
Figure 4. Linear extrapolation (the blue line) and quadratic interpolation (the red line) are used to approximate the ghost node acoustic pressure Pg.

Linear extrapolation is considered to reduce perturbations caused by points further below the surface such as PII. It needs two points to locally determine each ghost mirror point acoustic pressure Pg,m, which is located a distance ξR from the surface. Following from Figure 2, Figure 4 illustrates the linear extrapolation method. Thus, the ghost node's acoustic pressure Pg can be found using linear Lagrange extrapolation on values 0, and PI at positions 0 and ξD. We call it extrapolation because the distance ξR can be larger than ξD.

The hybrid method is a combination of the two previous methods. Depending on the location of the ghost mirror Pg,m (Figure 2), grid spacing Δz, and a tuning coefficient α, it independently determines whether to use linear extrapolation or quadratic interpolation for each ghost node. Algorithm 1 illustrates the hybrid method. The hybrid method uses linear extrapolation if the ghost mirror is between the surface and PI. However, if the ghost mirror is located between PI and PII, it decides whether to use linear extrapolation or quadratic interpolation depending on α, which ranges between zero and one. From the geometry in Figure 2, the maximum distance between PI and ghost mirror is Δz if the mirror is located between PI and PII. The hybrid method uses linear extrapolation if the ghost mirror is located between PI and PI+α*Δz; otherwise, if it falls between PI+α*Δz and PII, it uses quadratic interpolation.

Algorithm 1. Hybrid method used to determine whether to use linear extrapolation or quadratic interpolation for each ghost node.

Fourth-order scheme implementation

Due to the accuracy demands of the fourth-order finite-difference schemes, the acoustic-wave equation solution requires two layers of ghost nodes Pg above the surface. The first layer of ghost nodes is approximated using the hybrid method. The second layer of ghost nodes is located above the first layer. The acoustic pressures in the second layer are approximated using quadratic interpolation. Thus, three points are used to calculate the acoustic pressure at each ghost mirror Pg,m in the second layer. The first two points are PI and PII, which are found using bilinear interpolation. The third point PIII arises from extending the normal line further in the subsurface. Similarly, we use bilinear interpolation to approximate PIII. We also experimented using four points by including the zero acoustic pressure at the surface in addition to the three acoustic pressures PI, PII, and PIII. This will result in a Lagrange cubic interpolation. These two methods will be called the two-layer hybrid quadratic and cubic methods. We also experimented with only one hybrid layer by setting the second layer above the surface to zero. We call this the one-layer hybrid method.

RESULTS

We perform two simulations to test our embedded boundary methods for the second- and fourth-order finite-difference schemes (Petrov and Newman, 2012). The first simulation is done by solving the acoustic-wave equation in a homogeneous model with oblique planar topography. To measure the accuracy, we rotate the solution and compare the results with the analytical solution for a flat free-surface model (Aki and Richards, 2002; Pujol, 2003). The relative error e1 for the oblique planar topography is defined by

$$e_1(\mathbf{r}_{\partial\Omega}) = \frac{||P_{\text{sim}}(\mathbf{r}_{\partial\Omega})| - |P_A(\mathbf{r}_{\partial\Omega})||}{|P_A(\mathbf{r}_{\partial\Omega})|} \times 0100, \tag{11}$$

where $\mathbf{r}_{\partial\Omega} \in$ a surface $\partial\Omega$ that is parallel to the free surface, Psim is the simulation result, and PA is the analytical solution.

The second simulation addresses a homogeneous model with hill topography. Unlike the first simulation, there is no analytical solution for this case, and the relative error e2 is calculated relative to the maximum norm in the region Ω and is given by

$$e_2(\mathbf{r}_{\partial\Omega}) = \frac{|P_{\text{sim}}(\mathbf{r}_{\partial\Omega})|}{\max_{\mathbf{r}\in\Omega} |P_{\text{sim}}(\mathbf{r}_\Omega)|} \times 100, \tag{12}$$

where $\mathbf{r}_\Omega \in$ region Ω and the denominator denotes the maximum value in the region.

Oblique planar surface

In the oblique planar-surface case, we have a sloping surface in which we can rotate its solution to compare it with the analytical solution (see Figure 5). The surface is sloping 42° clockwise from the horizontal. The minimum distance between the Ricker-wavelet source and the sloping surface is 890 m. The complex frequency of the source is s=1+2i. We use the relative error e1 and average error ⟨e1⟩ to measure the accuracy of the oblique planar surface simulation.
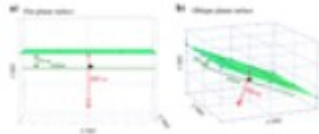

Figure 5. (a) The analytical free-surface case. The inline in the green is parallel to the flat surface. (b) The oblique planar free-surface case. The inline in green is parallel to the oblique planar surface. The grid spacing is 50 m, and the source denoted in red is 890 m below the surface.

For the second-order scheme, we will compare a finite-difference solution that includes staircasing of topography in the simulation, as well as the embedded boundary conditions, based on linear extrapolation, quadratic interpolation, and the hybrid method with α=0.95. We use a high tuning parameter α to bias the hybrid method to linear extrapolation. Most ghost mirror points are located closer to PI than PII, and thus linear extrapolation better approximates the ghost mirror pressure Pg,m than quadratic interpolation. For this comparison, we will implement a homogeneous media with P-wave velocity VP of 2250 m/s, density ρ of 2300kg/m^3, and grid spacing of 50 m. Figure 6a shows the relative error in pressure for the different simulation methods. All three embedded boundary methods provide accurate and similar results for the oblique planar surface relative to the true analytical solution. In general, the embedded boundary methods contain an average error of 1.3%, whereas the staircase methods have an average error of 28.5% (Table 1).

Table 1. The second-order finite-difference scheme for the acoustic-wave equation in homogeneous media with mesh size 70×74×85. The source frequency is 2 Hz with damping coefficient 1(1/s).
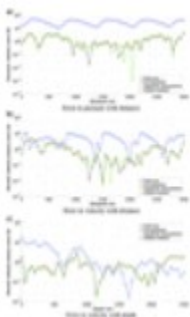

Figure 6. Error for the second-order finite-difference scheme staircase and embedded boundary methods relative to the true analytical solution.

To ensure that our method is continuous and differentiable, we study the pressure gradient. The results of the normal gradient (normal velocity

component) will be specifically illustrated because geophysical techniques measure normal velocity. Figure 6b and 6c shows that the average normal-velocity error for our embedded boundary methods is approximately 1% with respect to change in distance and depth.

Bohlen and Saenger (2006) conclude that to model topography with a staircase method, more than 60 grid points per minimum wavelength are required in a second-order scheme to obtain acceptable results. In Figure 7, we implemented an extreme case with approximately four points per wavelength at a frequency of 20 Hz with damping coefficient 1(1/s). To account for this increase in frequency, the velocity of the model was increased from 2250 to 3250m/s, and the grid spacing reduced from 50 to 15 m. The results show that our hybrid method produces results with an average error of approximately 3% when compared with the analytical solution (Figure 8).
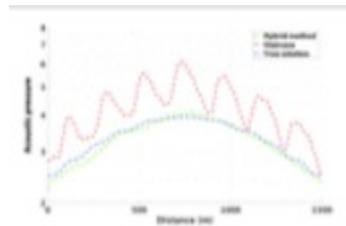
Figure 7. Absolute pressure for the second-order finite-difference scheme true, staircase, and hybrid method solutions. The plot demonstrates the solution 50 m below the surface for a frequency of 20 Hz with damping 1(1/s).
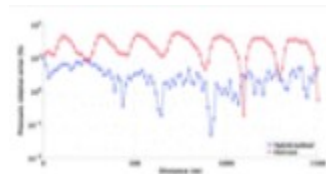

Figure 8. Relative error e1e1 for the second-order finite-difference scheme staircase and hybrid method acoustic pressure relative to the true analytical solution. The plot demonstrates the error 50 m below the surface for a frequency of 20 Hz with damping 1(1/s).

In the next numerical simulation, we demonstrate the solution of the acoustic-wave equation more accurately with a fourth-order finite-difference scheme. We use the same model setup as in the second-order finite-difference scheme. The model is illustrated in Figure 5 — it is homogeneous with P-wave velocity VP of 2250 m/s, density ρof 2300kg/m^3, and grid spacing of 50 m. The complex frequency of the source is s=1+2i. In this simulation, we compare the relative error in pressure between the staircase one- and two-layer hybrid methods with α=0.95. As shown in Figure 9, the two-layer method's average error is 1.3%. The one-layer method achieves an average accuracy of 5.4%. Similar to the previous simulation, the average accuracy of the staircase method is 23.5% (Table 2).

Table 2. The fourth-order finite-difference scheme for the acoustic-wave equation in a homogeneous media with mesh size 70×74×8570×74×85. The source frequency is 2 Hz with damping coefficient 1(1/s)1(1/s).
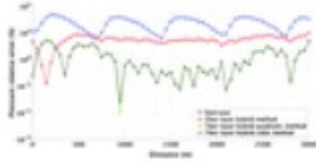
Figure 9. Relative error e1e1 for the fourth-order finite-difference scheme staircase and embedded boundary methods relative to the true analytical solution.

Hill model

To further measure the accuracy, we test our schemes on a hill surface. In terms of source type, source location, P-wave velocity, and density, the same configurations will be used as in the oblique planar simulations. As in the previous simulation, the complex frequency of the source is s=1+2i. We use relative error e2 and average error ⟨e2⟩ to measure the accuracy of the hill-surface simulation. Figure 10 illustrates the hill surface used for this experiment. The red lines denote profiles that will be studied in this section.
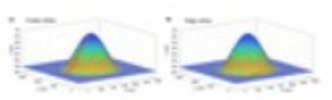

Figure 10. (a) Hill topography with the red line denoting the central line profile. (b) Hill topography with the red line denoting the edge line profile. The grid spacing is 50 m in all three components, and the source is located at (x,y,z)=(1200,1200,2600)m.

We use the second-order finite-difference scheme to the acoustic-wave equation. The tuning constant used for the hybrid method is α=0.95. We first start by comparing the central line profile shown in Figure 10a. Similar to the oblique planar simulation, all three embedded boundary methods have two orders of magnitude improvement over the staircase method (Table 1). Furthermore, all three embedded methods show approximately the same improvement (see Figure 11a). But for the edge line profile (Figure 10b), the linear extrapolation and the hybrid method provide more than two times better accuracy compared with the quadratic interpolation (Figure 11b and Table 1).
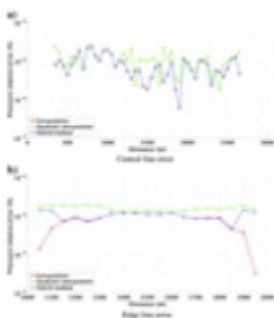

Figure 11. Relative error e2 for the second-order finite-difference scheme embedded boundary methods at the (a) central line shown in Figure 10a and (b) edge line shown in Figure 10b.

Spacing has been reduced for the staircase solution to demonstrate that when this happens, the higher resolution solution converges to the embedded-method solution with spacing of 50 m (Figure 12).
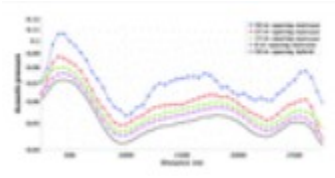
Figure 12. Absolute pressure solutions for the second-order finite-difference scheme embedded boundary methods with different spacings for the hill model central line at 50 m below the surface.

To study the effectiveness of our curvature method, we stretched the hill model to have a height of 1500 m instead of the 700 m in Figure 10. In Figure 13, we show that when the edge-line curvature radius is small, the error for the solution with curvature correction is reduced by up to two times compared with the error for the solution without the curvature correction.
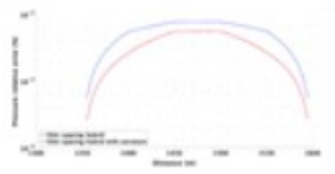

Figure 13. Relative error e2 for the second-order finite-difference scheme embedded boundary methods at the edge line for a stretched hill with height 1500 m.

In Figure 14, we implemented an extreme case with approximately four points per wavelength at frequency 20 Hz with damping coefficient 1(1/s). The velocity and spacing have been changed as in the oblique planar case. The results show that our hybrid method produces results with two orders of magnitude improvement over the staircase method with frequency 20 Hz (Figure 15).
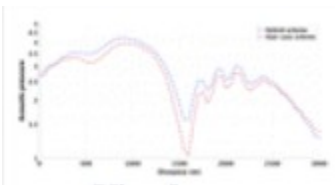

Figure 14. Absolute pressure for the second-order finite-difference scheme embedded boundary methods at the central line shown in Figure 10a at 100 m below the surface. The plot demonstrates the solutions for a frequency of 20 Hz with damping 1(1/s).
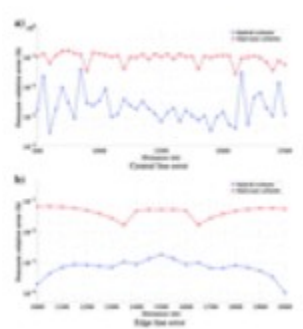

Figure 15. Relative error e2 for the second-order finite-difference scheme embedded boundary methods at the (a) central line shown in Figure 10a and (b) edge line shown in Figure 10b. The plot demonstrates the error for a frequency of 20 Hz with damping 1(1/s).

Now, the acoustic-wave equation is solved using a fourth-order finite-difference scheme. We compare solutions for the central line and edge line profiles shown in Figure 10. Contrary to the oblique-planar model simulation, Figure 16 only shows marginal improvement when using the two-layer hybrid methods over the one-layer hybrid method (Table 2).
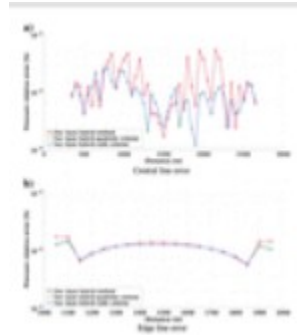

Figure 16. Relative error e2 for the fourth-order finite-difference scheme embedded boundary methods at the (a) central line shown in Figure 10a and (b) edge line profile shown in Figure 10b.

Solver convergence rates

Efficient convergence rates are essential for solving the forward problem because it is the driving engine in the solution of the inverse problem. Thus, the forward problem will be solved many times to reach the best-fit model for the data. Here, we study the convergence rates to decide which embedded boundary method is more computationally efficient. All the tests were conducted on a 2013 MacBook Pro with a 2.4 GHz dual-core Intel i5 processor, 3 MB shared L3 cache, and 8 GB of 1600MHz DDR3L onboard memory. We use a Krylov subspace induced dimension reduction (IDR) iterative solver to solve the forward model at interior nodes (Sonneveld and van Gijzen, 2008). Direct solvers can also be used for small simulations or as a preconditioner for the iterative solver.

We start the first set of tests with second-order finite-difference schemes for a homogeneous medium. We compare between different topographies and embedded boundary methods. For the oblique-planar surface, there is no considerable difference in terms of number of iterations or convergence rate (Table 1). It is better to use the linear extrapolation method because it is slightly more accurate. However, the hill irregular surface shows a spike in the number of iterations and a corresponding increase in time for the linear extrapolation solution (Table 1). We have observed that the linear extrapolation takes more time to converge when there are more ghost points closer to PII than PI. Thus, it is more efficient to implement the hybrid method with $\alpha=0.95$. The hybrid-method results are similar in accuracy to the linear extrapolation but have better convergence rates as shown in Table 1. On the other hand, the quadratic interpolation is faster but has marginally less accuracy.

Because linear extrapolation is accurate but inefficient and quadratic interpolation is efficient but not as accurate, we experimented with different

tuning ratios α to find the best compromise in efficiency and accuracy. In Figure 17, we show that α=0.95 provides a good trade-off. It is accurate relative to the linear extrapolation (α=1) and also efficient, as shown in Table 1.
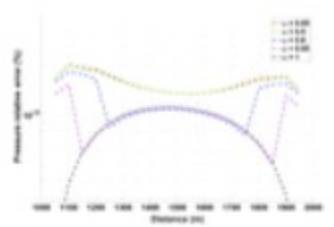

Figure 17. Relative error e2 for the second-order finite-difference scheme hybrid method at the edge line for different tuning ratios α.

We compare tests for the fourth-order finite-difference schemes for a homogeneous medium. In these tests, we compare between the one- and two-layer hybrid methods as shown in Table 2. For the oblique-planar and hill surfaces, the two-layer hybrid quadratic method is approximately 10 times slower than the one-layer hybrid method. Despite its slightly less accurate solution, the one-layer hybrid method is substantially more time efficient than the two-layer hybrid quadratic method. However, using a two-layer hybrid cubic method can reduce time inefficiencies. In fact, for the central hill profile, the solution times for the two-layer hybrid cubic are comparable with the one-layer hybrid method.

CONCLUSION

We report improved embedded boundary methods for 3D acoustic seismic wave-propagation modeling when arbitrarily free-surface topography is present. Unlike the classic staircase method and finite-difference algorithms that use structured curvilinear body-fitted grids, our embedded boundary methods — quadratic interpolation, linear extrapolation, and one- and two-layer hybrid — use a regular Cartesian grid system, which greatly simplifies mesh generation and omits the need to change our current finite-difference formalizations. The free-surface boundary is enforced at the actual surface locations through the method of images, allowing for an accurate representation of an arbitrary free-surface geometry. As demonstrated with numerical experiments, our embedded methods significantly reduce the staircasing error. Our results showed that the hybrid method is efficient in terms of accuracy and performance for second-order finite difference, whereas the two-layer hybrid cubic method is more efficient for fourth-order finite-difference implementation. These methods are designed to choose between linear extrapolation and quadratic interpolation according to a tolerance variable without adversely affecting performance. We use a high tuning parameter αα to bias the hybrid method to linear extrapolation, for the increase in accuracy that linear extrapolation achieves over quadratic interpolation. Previous published works only take quadratic interpolation into consideration, which makes their embedded methods dependent on nodes

further below the surface. Our results show that linear extrapolation that depends on nodes close to the surface can produce better results. It achieves slightly more accurate results when compared with quadratic interpolation for the oblique planar surface. For the hill irregular surface, it is about two times better than quadratic interpolation. These algorithms can handle any surface topography under a regular Cartesian coordinate system. Therefore, they have significant potential to become a powerful part of a forward-modeling engine used for full-waveform inversion.

ACKNOWLEDGMENTS

REFERENCES

Aki, K., and P. G. Richards, 2002, *Quantitative seismology*, 2nd ed.: University Science Books.

Bohlen, T., and E. H. Saenger, 2006, Accuracy of heterogeneous staggered-grid finite-difference modeling of Rayleigh waves: *Geophysics*, 71, no. 4, T109–T115, doi: https://doi.org/10.1190/1.2213051.

Fichtner, A., 2011, *Full seismic waveform modelling and inversion*: Springer.

Gottschammer, E., and K. Olsen, 2001, Accuracy of the explicit planar free-surface boundary condition implemented in a fourth-order staggered-grid velocity-stress finite-difference scheme: *Bulletin of the Seismological Society of America*, 91, 617–623, doi: https://doi.org/10.1785/0120000244.

Graves, R. W., 1996, Simulating seismic wave propagation in 3D elastic media using staggered-grid finite differences: *Bulletin of the Seismological Society of America*, 86, 1091–1106.

Griffiths, D. J., 2005, *Introduction to electrodynamics*: AAPT.

Hastings, F. D., J. B. Schneider, and S. L. Broschat, 1996, Application of the perfectly matched layer (PML) absorbing boundary condition to elastic wave propagation: *The Journal of the Acoustical Society of America*, 100, 3061–3069, doi: https://doi.org/10.1121/1.417118.

Hestholm, S., 1999, Three-dimensional finite difference viscoelastic wave modelling including surface topography: *Geophysical Journal International*, 139, 852–878, doi: https://doi.org/10.1046/j.1365-246x.1999.00994.x.

Hestholm, S., and B. Ruud, 2000, 2D finite-difference viscoelastic wave modelling including surface topography: *Geophysical Prospecting*, 48, 341–373, doi: https://doi.org/10.1046/j.1365-2478.2000.00185.x.

Hustedt, B., S. Operto, and J. Virieux, 2004, Mixed-grid and staggered-grid finite-difference methods for frequency-domain acoustic wave modelling:

Geophysical Journal International, 157, 1269–1296, doi:https://doi.org/10.1111/j.1365-246X.2004.02289.x.

Jackson, J. D., 2007, *Classical electrodynamics*: John Wiley & Sons.

Jo, C.-H., C. Shin, and J. H. Suh, 1996, An optimal 9-point, finite-difference, frequency-space, 2D scalar wave extrapolator: *Geophysics*, 61, 529–537, doi: https://doi.org/10.1190/1.1443979.

Kim, S., and J. E. Pasciak, 2010, Analysis of a Cartesian PML approximation to acoustic scattering problems in R2: *Journal of Mathematical Analysis and Applications*, 370, 168–186, doi:https://doi.org/10.1016/j.jmaa.2010.05.006.

Kreiss, H.-O., and N. A. Petersson, 2006, An embedded boundary method for the wave equation with discontinuous coefficients: *SIAM Journal on Scientific Computing*, 28, 2054–2074, doi:https://doi.org/10.1137/050641399.

Levander, A. R., 1988, Fourth-order finite-difference P-SV seismograms: *Geophysics*, 53, 1425–1436, doi:https://doi.org/10.1190/1.1442422.

Li, J., Y. Zhang, and M. N. Töksoz, 2010, Frequency-domain finite-difference acoustic modeling with free surface topography using embedded boundary method: 80th Annual International Meeting, SEG, Expanded Abstracts, 2966–2971.

Lombard, B., J. Piraux, C. Gélis, and J. Virieux, 2008, Free and smooth boundaries in 2D finite-difference schemes for transient elastic waves: *Geophysical Journal International*, 172, 252–261, doi:https://doi.org/10.1111/j.1365-246X.2007.03620.x.

Lysmer, J., and L. A. Drake, 1972, A finite element method for seismology: *Methods in Computational Physics*, 11, 181–216.

Marfurt, K. J., 1984, Accuracy of finite-difference and finite-element modeling of the scalar and elastic wave equations: *Geophysics*, 49, 533–549, doi: https://doi.org/10.1190/1.1441689.

Morse, P. M., and H. Feshbach, 1954, *Methods of theoretical physics*: AAPT.

Ohminato, T., and B. A. Chouet, 1997, A free-surface boundary condition for including 3D topography in the finite-difference method: *Bulletin of the Seismological Society of America*, 87, 494–515.

Operto, S., J. Virieux, P. Amestoy, J.-Y. L'Excellent, L. Giraud, and H. B. H. Ali, 2007, 3D finite-difference frequency-domain modeling of visco-acoustic wave propagation using a massively parallel direct solver: A feasibility study: *Geophysics*, 72, no. 5, SM195–SM211, doi: https://doi.org/10.1190/1.2759835.

Petrov, P. V., and G. A. Newman, 2012, 3D finite-difference modeling of elastic wave propagation in the laplace-fourier domain: *Geophysics*, 77, no. 4, T137–T155, doi: https://doi.org/10.1190/geo2011-0238.1.

Pratt, R. G., and M. Worthington, 1990, Inverse theory applied to multi-source cross-hole tomography — Part 1: Acoustic wave-equation method: *Geophysical Prospecting*, 38, 287–310, doi:https://doi.org/10.1111/j.1365-2478.1990.tb01846.x.

Pujol, J., 2003, *Elastic wave propagation and generation in seismology*: Cambridge University Press.

Rheinboldt, W. C., 1998, *Methods for solving systems of nonlinear equations*: SIAM.

Sonneveld, P., and M. B. van Gijzen, 2008, IDR (s): A family of simple and fast algorithms for solving large nonsymmetric systems of linear equations: *SIAM Journal on Scientific Computing*, 31, 1035–1062, doi:https://doi.org/10.1137/070685804.

Spivak, M., 1981, *Comprehensive introduction to differential geometry*: Publish or Perish Inc., University of Tokyo Press vol. iv.[a].

Štekl, I., and R. G. Pratt, 1998, Accurate viscoelastic modeling by frequency-domain finite differences using rotated operators: *Geophysics*, 63, 1779–1794, doi: https://doi.org/10.1190/1.1444472.

Tessmer, E., and D. Kosloff, 1994, 3D elastic modeling with surface topography by a Chebychev spectral method: *Geophysics*, 59, 464–473, doi: https://doi.org/10.1190/1.1443608.

Tessmer, E., D. Kosloff, and A. Behle, 1992, Elastic wave propagation simulation in the presence of surface topography: *Geophysical Journal International*, 108, 621–632, doi: https://doi.org/10.1111/j.1365-246X.1992.tb04641.x

Virieux, J., 1986, P-sv wave propagation in heterogeneous media: Velocity-stress finite-difference method: *Geophysics*, 51, 889–901, doi: https://doi.org/10.1190/1.1442147.

Zahradník, J., P. Moczo, and F. Hron, 1993, Testing four elastic finite-difference schemes for behavior at discontinuities: *Bulletin of the Seismological Society of America*, 83, 107–129.

Zahradník, J., and L. Urban, 1984, Effect of a simple mountain range on underground seismic motion: *Geophysical Journal International*, 79, 167–183, doi: https://doi.org/10.1111/j.1365-246X.1984.tb02848.x.

Zhang, W., and X. Chen, 2006, Traction image method for irregular free surface boundaries in finite difference seismic wave simulation: *Geophysical Journal International*, 167, 337–353, doi:https://doi.org/10.1111/j.1365-246X.2006.03113.x.

Zhang, W., Z. Zhang, and X. Chen, 2012, Three-dimensional elastic wave numerical modelling in the presence of surface topography by a collocated-grid finite-difference method on curvilinear grids: *Geophysical Journal*

APPENDIX APIECEWISE FREE-SURFACE EQUATION

Using topography data points Ti,j, a piecewise quadratic topography equation fi,j(x,y) is approximated. The quadratic approximation in multiple variables is given by

fi,j(x,y)≈fi,j(x0,y0)+∂xfi,j(x0,y0)(x−x0)+∂yfi,j(x0,y0)(y−y0)+12! (
[∂xxfi,j(x0,y0)(x−x0)2+2∂xyfi,j(x0,y0)(x−x0)(y−y0)+∂yyfi,j(x0,y0) A-
(y−y0)2], 1)

where fi,j(x,y) is the approximated topography equation for the surface about the point (x0,y0) and the symbols ∂x, ∂y, ∂xx, ∂xy, and ∂yy, respectively, denote the partial differential operators ∂/∂x, ∂/∂y, ∂2/∂x, ∂2/∂x∂y, and ∂2/∂y2, respectively. Furthermore, the piecewise equation A-1 is bounded by

{xi−1<x<xi+1yi−1<y<yi+1. (A-2)

where i and j are the indices of the topography nodes. Thus, xi corresponds to i·Δx and yj corresponds to j·Δy. The coefficients of equation A-1 are found by the central finite-difference relationships. We use topography data points to calculate the coefficients of the equation:

∂xfi,j(x,y)≈Ti+1,j−Ti−1,j2Δx,∂yfi,j(x,y)≈Ti,j+1−Ti,j−12Δy,∂xxfi,j(x,y)≈Ti (A-3)
+1,j−2Ti,j+Ti−1,jΔx2,∂xyfi,j(x,y)≈Ti+1,j+1−Ti−1,j+1−Ti+1,j−1+Ti−1,j
−14ΔxΔy,∂yyfi,j(x,y)≈Ti,j+1−2Ti,j+Ti,j−1Δy2.